

# Molecular chemistry induced by J-shock toward supernova remnant W51C

Tian-Yu Tu<sup>1</sup>, Valentine Wakelam<sup>2</sup>, Yang Chen<sup>1,3</sup>, Ping Zhou<sup>1,3</sup>, and Qian-Qian Zhang<sup>1</sup>

<sup>1</sup> School of Astronomy & Space Science, Nanjing University, 163 Xianlin Avenue, Nanjing 210023, China  
e-mail: ygchen@nju.edu.cn

<sup>2</sup> Laboratoire d'Astrophysique de Bordeaux, Univ. Bordeaux, CNRS, B18N, allée Geoffroy Saint-Hilaire, 33615 Pessac, France

<sup>3</sup> Key Laboratory of Modern Astronomy and Astrophysics, Nanjing University, Ministry of Education, Nanjing 210023, China

Received ...; accepted ...

## ABSTRACT

**Context.** Shock waves from supernova remnants (SNRs) have strong influence on the physical and chemical properties of molecular clouds (MCs). Shocks propagating into magnetized MCs can be classified into “jump” J-shock and “continuous” C-shock. The molecular chemistry in the re-formed molecular gas behind J-shock is still not well understood, which will provide a comprehensive view of the chemical feedback of SNRs and the chemical effects of J-shock.

**Aims.** We conducted a W-band (71.4–89.7 GHz) observation toward a re-formed molecular clump behind a J-shock induced by SNR W51C with the Yebes 40 m radio telescope to study the molecular chemistry in the re-formed molecular gas.

**Methods.** Based on the local thermodynamic equilibrium (LTE) assumption, we estimate the column densities of HCO<sup>+</sup>, HCN, C<sub>2</sub>H and *o-c*-C<sub>3</sub>H<sub>2</sub>, and derive the maps of their abundance ratios with CO. The gas density is constrained by non-LTE analysis of the HCO<sup>+</sup> *J* = 1–0 line. The abundance ratios are compared with the values in typical quiescent MCs and shocked MCs, and are also compared with the results of chemical simulations with the Paris-Durham shock code to verify and investigate the chemical effects of J-shock.

**Results.** We obtain the following abundance ratios:  $N(\text{HCO}^+)/N(\text{CO}) \sim (1.0\text{--}4.0) \times 10^{-4}$ ,  $N(\text{HCN})/N(\text{CO}) \sim (1.8\text{--}5.3) \times 10^{-4}$ ,  $N(\text{C}_2\text{H})/N(\text{CO}) \sim (1.6\text{--}5.0) \times 10^{-3}$ , and  $N(o\text{-}c\text{-C}_3\text{H}_2)/N(\text{CO}) \sim (1.2\text{--}7.9) \times 10^{-4}$ . The non-LTE analysis suggests that the gas density is  $n_{\text{H}_2} \gtrsim 10^4 \text{ cm}^{-3}$ . We find that the  $N(\text{C}_2\text{H})/N(\text{CO})$  and  $N(o\text{-}c\text{-C}_3\text{H}_2)/N(\text{CO})$  are higher than typical values in quiescent MCs and shocked MCs by 1–2 orders of magnitude, which can be qualitatively attributed to the abundant C<sup>+</sup> and C at the earliest phase of molecular gas re-formation. The Paris-Durham shock code can reproduce, although not perfectly, the observed abundance ratios, especially the enhanced  $N(\text{C}_2\text{H})/N(\text{CO})$  and  $N(o\text{-}c\text{-C}_3\text{H}_2)/N(\text{CO})$ , with J-shocks propagating in to both non-irradiated and irradiated molecular gas with a preshock density of  $n_{\text{H}} = 2 \times 10^3 \text{ cm}^{-3}$ .

**Key words.** shock waves – ISM: molecules – ISM: clouds – ISM: supernova remnants – ISM: individual objects: W51C

## 1. Introduction

Supernova remnants (SNRs) exert strong influence on the physical and chemical properties of the molecular clouds (MCs) they interact with (e.g., van Dishoeck et al. 1993). Among all the effects driven by SNRs, the shock waves play a crucial role. Shock can heat, compress and accelerate the molecular gas (Draine & McKee 1993), altering the physical properties of the MC, and regulate the molecular chemistry through various processes (e.g., Burkhardt et al. 2019).

Shocks propagating into magnetized MCs can be roughly classified into two types: J-shocks and C-shocks (Draine & McKee 1993). J-shocks, where J refers to “jump”, are often fast and weakly magnetized. The deceleration and heating of the entire shock is almost entirely due to the viscous stresses arising in a thin transition layer called the viscous subshock. A jump of physical parameters (density, temperature, etc.) is expected in the shock profile. On the contrary, C-shocks, where C refers to “continuous”, are often slow and strongly magnetized. The momentum transfer and heating are finished by the magnetic precursor which goes ahead of the viscous subshock when the magnetic field is strong enough to make the magnetosonic speed ( $B/\sqrt{4\pi\rho_i}$ ) higher than the shock velocity. Therefore, the physi-

cal parameters change continuously without a jump between the upstream and downstream.

Molecular chemistry induced by C-shocks has been extensively studied in SNRs (e.g., van Dishoeck et al. 1993; Lazendic et al. 2010; Zhou et al. 2022; Tu et al. 2024a) and other astrophysical environments such as molecular outflows of protostars (e.g., Bachiller et al. 2001; Mendoza et al. 2018; Codella et al. 2020). Since C-shocks are non-dissociative, most molecules can survive, and C-shocks can also release the depleted molecular species back to the gas phase and make them detectable (e.g., SiO, Gusdorf et al. 2008). However, investigations of molecular chemistry induced by J-shock are hampered by the fact that J-shock can result in much higher temperature than C-shock and most molecules will be dissociated (e.g., Kristensen et al. 2023). Therefore, observational studies of J-shock often turn to emission lines of atoms (e.g., Rho et al. 2001; Lee et al. 2019) or infrared transitions of a limited variety of molecules: CO, H<sub>2</sub> and H<sub>2</sub>O (e.g., Shinn et al. 2012; Rho et al. 2015). However, simulations have found that molecules can re-form in the cooling gas behind a fast and dissociative J-shock (Hollenbach & McKee 1989; Neufeld & Dalgarno 1989; Cuppen et al. 2010; Hollenbach et al. 2013), and observations have also found this re-formed molecular gas in SNRs W51C (Koo & Moon 1997b)

and IC443 (Wang & Scoville 1992). In the prototypical protostellar outflow L1157, molecular gas re-formed behind J-shock was identified by CO observations (Lefloch et al. 2012; Benedettini et al. 2012), and re-formed CS was discovered (Gómez-Ruiz et al. 2015). However, the abundance of CS deviates little from other C-shocked components. It is still unclear whether J-shock can induce different chemistry compared with C-shock and quiescent gas conditions.

SNR W51C (G49.2–0.7) is a middle-aged SNR interacting with MCs, evidenced by 1720 MHz OH masers (Green et al. 1997), broadened molecular line (Koo & Moon 1997b; Brogan et al. 2013), SiO emission (Dumas et al. 2014), etc. The cold CO gas re-formed behind a J-shock was found by Koo & Moon (1997b) based on three observational facts. First, the local-standard-of-rest (LSR) velocity of the CO gas ( $\gtrsim 80 \text{ km s}^{-1}$ ) is larger than the tangent point LSR velocity ( $\approx 60 \text{ km s}^{-1}$ ) toward this direction ( $l \approx 49^\circ$ ), so it is likely that the CO gas is accelerated by the shock to high LSR velocity. Second, the line-of-sight velocity separation between the preshock and postshock CO gas is large ( $\approx 20\text{--}50 \text{ km s}^{-1}$ ), while for C-shock, the postshock gas should be at velocities closer to that of the preshock gas since the acceleration of the shocked gas is continuous. Third, the estimated excitation temperature of the CO emission is low ( $\sim 10 \text{ K}$ ), which should be higher for C-shocked gas. Fourth, the postshock CO gas exhibits spatial and spectral coincidence with high-velocity HI gas which has been proposed to be subject to a fast shock with a velocity of  $\sim 100 \text{ km s}^{-1}$  (Koo & Moon 1997a).

In this work, we present our new molecular observation toward the “clump 2” of W51C found and named by Koo & Moon (1997b) to study the detailed molecular chemistry induced by J-shock. In Section 2, we describe the details about our observation and data reduction. The observational results are presented in Section 3. In Section 4, we calculate the molecular column densities and abundance ratios, constrain the gas density, discuss the chemistry of carbon chain species, and present the results of chemical simulation. Our conclusions are summarized in Section 5.

## 2. Observations

### 2.1. Yebes 40 m observation

We conducted new mapping observation toward clump 2 (which was identified and named by Koo & Moon (1997b)) of SNR W51C with the Yebes 40 m radio telescope (PI: Tian-Yu Tu, project code: 24A003) in W-band covering a spectral range of 71.4–89.7 GHz. Position switching mode was adopted throughout the observation with the reference point at  $\alpha_{J2000} = 19^{\text{h}}23^{\text{m}}05^{\text{s}}.8$ ,  $\delta_{J2000} = +14^\circ 10' 56''$ . The mapping was made toward a  $82''.5 \times 82''.5$  region centered at  $\alpha_{J2000} = 19^{\text{h}}22^{\text{m}}45^{\text{s}}.69$ ,  $\delta_{J2000} = +14^\circ 11' 58''.9$  in a pixel size of  $7''.5 \times 7''.5$  (see Figure 1 for the position and size of the mapped region). The sensitivity measured in main beam temperature  $T_{\text{mb}}$  at the raw spectral resolution (38 kHz) is 0.05–0.09 K. The data was reduced with the GILDAS/CLASS package<sup>1</sup>. For better comparison, all of the reduced data cubes are smoothed to a common beam size of  $27''.6$ .

### 2.2. Other archival data

We obtained some archival data to support our analysis. The  $^{12}\text{CO } J = 3\text{--}2$  data was retrieved from the  $^{12}\text{CO } (3\text{--}2)$  High-Resolution Survey (COHRS) project (Park et al. 2023) per-

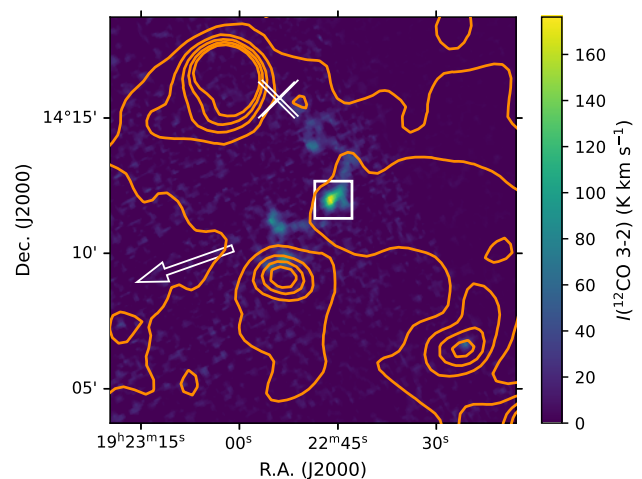


**Fig. 1.** Integrated intensity map of the JCMT  $^{12}\text{CO } J = 3\text{--}2$  line in velocity range  $+80\text{--}+110 \text{ km s}^{-1}$ , which is the velocity range of the re-formed CO gas proposed by Koo & Moon (1997b), overlaid with orange contours of VGPS 1.4 GHz radio continuum (levels are 50–250 K in steps of 50 K). The two white crosses shows the 1720 MHz OH masers discovered by Green et al. (1997). The white arrow points to the geometric center of W51C recorded in the Green’s SNR catalog (Green 2019). The white box shows the molecular clump toward which we conducted the Yebes 40 m observation.

formed by the James Clarke Maxwell Telescope (JCMT). The angular resolution is  $16.6''$  and the sensitivity measured in  $T_{\text{A}}^*$  is  $\sim 1 \text{ K}$  at a velocity channel width of  $0.635 \text{ km s}^{-1}$ . The antenna temperature was converted to  $T_{\text{mb}}$  with a main beam efficiency of 0.61.

We also obtained the  $^{12}\text{CO } J = 1\text{--}0$  data observed by the Nobeyama 45 m telescope and the [C I] ( $^3P_1\text{--}^3P_0$ ) data observed by the Atacama Submillimeter Telescope Experiment (ASTE) 10 m telescope from Yamagishi et al. (2023). Details of the observation can be found therein. All of these supplementary data cubes are smoothed to a beam size of  $27''.6$ .

The 1.4 GHz radio continuum map of W51C was obtained from the VLA Galactic Plane Survey (VGPS, Stil et al. 2006). All the processed data were further analyzed with *Python* packages Astropy (Astropy Collaboration et al. 2018, 2022) and Spectral-cube<sup>2</sup>. The data cubes of the CO isotopes were reprojected with the reproject<sup>3</sup> package. We visualized the data with *Python* package Matplotlib<sup>4</sup>.

## 3. Results

In total, we detected transitions from 24 molecular species, among which five ( $\text{HCO}^+$ , HCN,  $\text{C}_2\text{H}$ ,  $o\text{-}c\text{-C}_3\text{H}_2$ , and  $\text{H}_2\text{CO}$ ) show broadened emission line profiles in velocity range  $+80\text{--}+110 \text{ km s}^{-1}$ , which is the LSR velocity range of the re-formed CO gas (Koo & Moon 1997b), while others are only detected around  $\sim +61 \text{ km s}^{-1}$  which corresponds to the ambient MCs. The spectra of the five molecular transitions averaged in the entire mapped region, together with the  $^{12}\text{CO}$  (hereafter CO if not specified)  $J = 1\text{--}0$  and  $3\text{--}2$  lines, are shown in Figure 2. The averaged spectra of other detected molecular species are shown in Appendix A. The  $\text{HCO}^+$  and HCN lines exhibit the highest

<sup>2</sup> <https://spectral-cube.readthedocs.io/en/latest/>

<sup>3</sup> <https://reproject.readthedocs.io/en/stable/>

<sup>4</sup> <https://matplotlib.org/>

<sup>1</sup> <https://www.iram.fr/IRAMFR/GILDAS/>

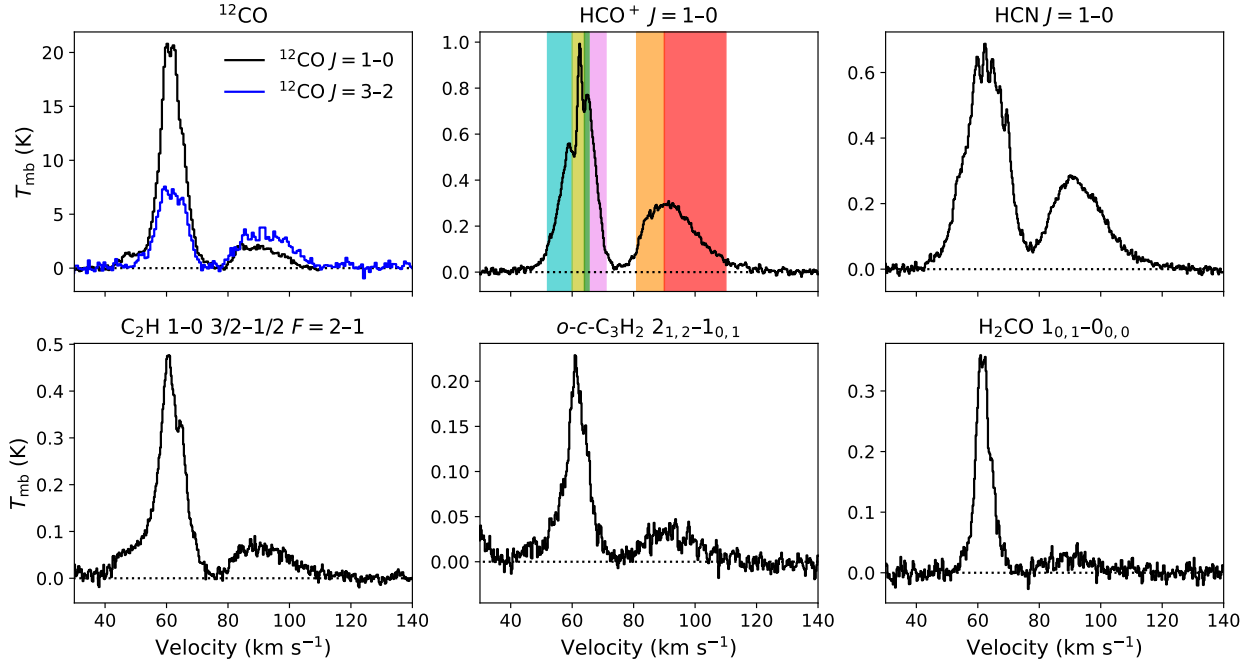


**Fig. 2.** Spectra of the molecular transitions with emission detected in velocity range +80–+110 km s<sup>-1</sup> averaged across the entire mapped region. Velocity integration intervals for the six velocity components are shown by colored rectangles in the spectrum of HCO<sup>+</sup>.

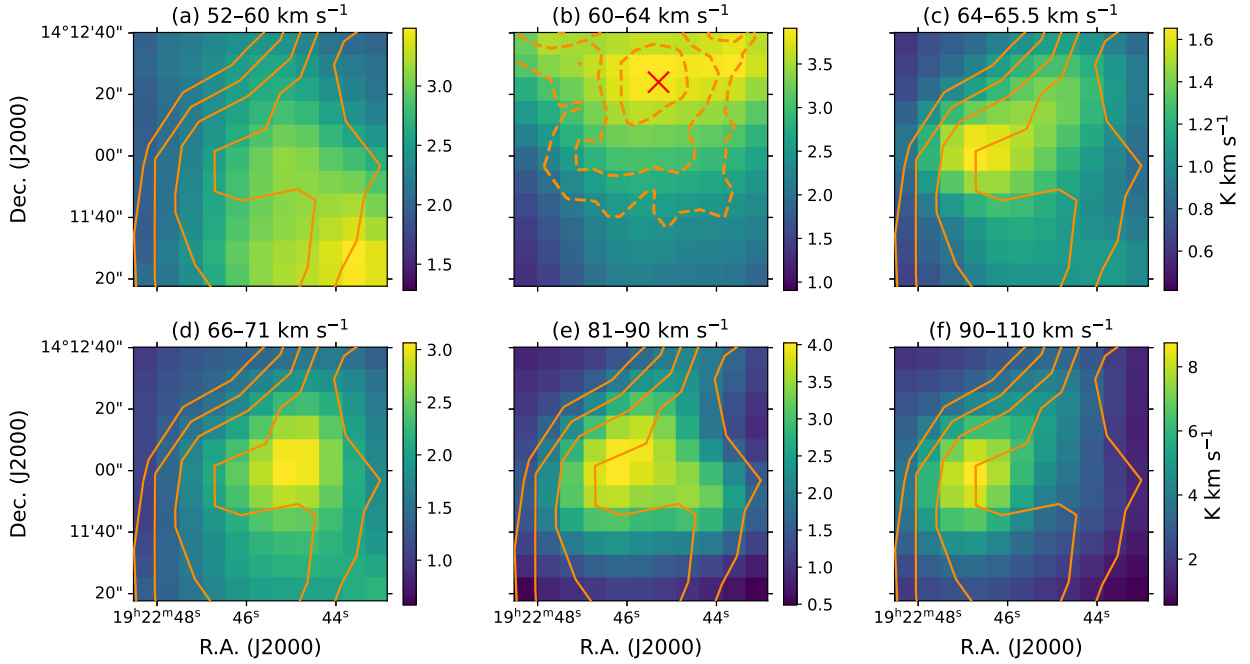


**Fig. 3.** HCO<sup>+</sup> Integrated intensity map of the six velocity components marked by colored rectangles in Figure 2. The solid orange contours show the VGPS 1.4 GHz radio continuum at 104–112 K levels in steps of 2 K from left (east) to right (west), while the dashed orange contours show the ATLASGAL 870 μm continuum (in steps of 0.3, 0.6 and 0.9 Jy beam<sup>-1</sup>). The red cross in panel (b) shows the position of ATLASGAL clump G49.111–0.322.

signal-to-noise ratio. Considering that the HCN line may be affected by the hyperfine structures, we use the HCO<sup>+</sup> line to analyze the velocity structure in the mapped region.

We divided the entire HCO<sup>+</sup> spectrum into six components (see the colored rectangles in Figure 2) based on visual inspections on their spatial distributions. The integrated intensity map of the six components are shown in Figure 3. Component (a) is bright toward the southwest of the mapped region and does not

show spatial coincidence with the radio continuum. Component (b) is mainly located in the north and is spatially coincident with the 870 μm far-infrared continuum dust emission detected by the the APEX Telescope Large Area Survey of the GALaxy (ATLASGAL, Urquhart et al. 2018). The emission peak of HCO<sup>+</sup> in this component is also consistent with the ATLASGAL clump G49.111–0.322. Components (c) and (d) are contiguous in the spectrum: (c) is an emission peak while (d) exhibits a line wing

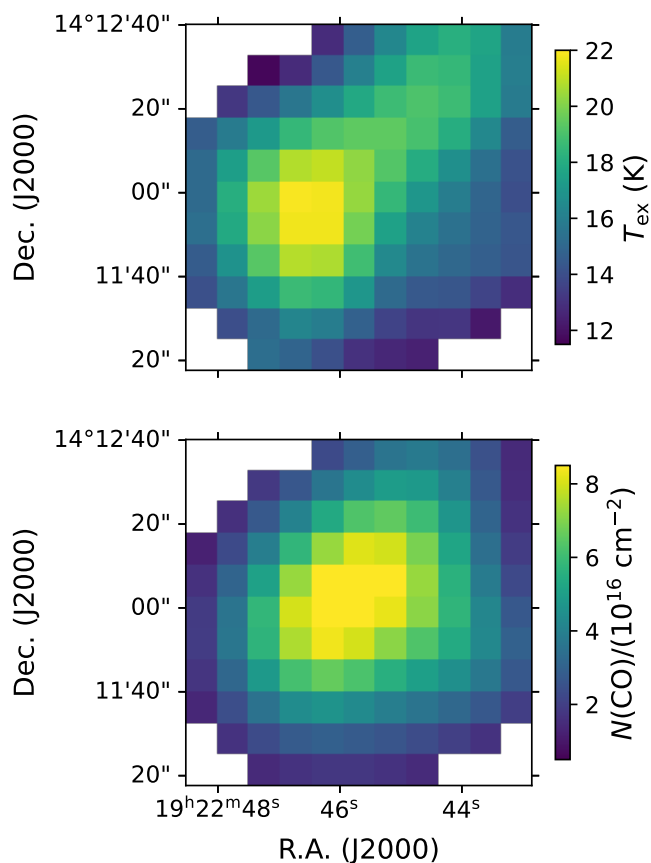


**Fig. 4.** Excitation temperature (upper panel) and column density (lower panel) maps of CO.

structure (see Figure 2). However, component (c) is located toward the east of (d) and is spatially coincident with a bulge of radio continuum. Both components could be preshock gas of W51C or C-shocked gas. Components (e) and (f) are separated from the other velocity components and have been proposed to be the molecular gas re-formed behind fast J-shock. However, these two components show slightly different spatial distribution. The majority of the emission in component (e) is toward the center of the mapped region, while this component also contains a weak emission feature toward the west. For component (f), the emission toward the west vanishes, while the emission peak moves east compared with component (e). The spatial distribution of component (f) is similar to (c) and is also coincident with a bulge of radio continuum.

Although the re-formed gas can be divided into two velocity components, it is hard to perform spectral decomposition because the shocked gas does not necessarily exhibit Gaussian line profile and the signal-to-noise ratio of other transitions are limited. In the following analysis, we regard the two components as one. We also note that none of components (a) to (d) can be undoubtedly identified as the preshock gas. Besides, a pixel-by-pixel decomposition of all the observed spectra around  $61 \text{ km s}^{-1}$  is almost impossible. Therefore, we cannot estimate the properties of the preshock gas directly from our observation.

## 4. Discussion

### 4.1. Estimation of the molecular column densities and abundance ratios

Considering that we do not have the data of multiple ( $\geq 3$ ) transitions of one molecular species, we assume local thermodynamic equilibrium (LTE) in our estimation of the molecular column densities. We assume that all the transitions in velocity range  $+80$ – $+110 \text{ km s}^{-1}$  are optically thin because of their large linewidths which in turn suggest large velocity gradients. The excitation temperature ( $T_{\text{ex}}$ ) of the CO lines can be estimated by fitting the relation (Goldsmith & Langer 1999):

$$\log \frac{N_u}{g_u} = \log N - \log Z - \frac{E_u}{kT_{\text{ex}}} \quad (1)$$

where  $N_u$  is the column density of the molecules in the upper energy level,  $g_u$  is statistical weight of the upper energy level,  $N$  is the total column density,  $Z$  is the partition function, and  $E_u$  is the energy of the upper level. In the optical thin limit,  $N_u$  can be written as  $N_u = (8\pi k\nu^2 W)/(hc^3 A_{ul})$  where  $W$  is the integrated intensity and  $A_{ul}$  is the Einstein  $A$  coefficient of the transition. With  $T_{\text{ex}}$  obtained, the column density can be estimated via (Mangum & Shirley 2015):

$$N = \frac{3k}{8\pi^3\nu} \frac{Z \exp(E_u/kT_{\text{ex}})}{S\mu^2} \frac{J_\nu(T_{\text{ex}})}{J_\nu(T_{\text{ex}}) - J_\nu(T_{\text{bg}})} W, \quad (2)$$

where  $S$  is the line strength,  $\mu$  is the dipole moment,  $T_{\text{bg}} = 2.73 \text{ K}$  is the background temperature, and  $J_\nu(T)$  is defined by  $J_\nu(T) = (h\nu/k)/(\exp(h\nu/kT) - 1)$ . The molecular constants ( $E_u$  and  $S\mu^2$ ) are retrieved from Splatalogue<sup>5</sup>. The obtained  $T_{\text{ex}}(\text{CO})$  and  $N(\text{CO})$  maps are shown in Figure 4. Generally, the  $T_{\text{ex}}(\text{CO})$  is within the range 11.5–23 K, and the  $N(\text{CO})$  is within  $1$ – $9 \times 10^{16} \text{ cm}^{-2}$  throughout the clump. The peaks of both values are higher than those obtained by Koo & Moon (1997a), which are  $T_{\text{ex}} = 11 \text{ K}$  and  $N(\text{CO}) = 4 \times 10^{16} \text{ cm}^{-2}$ , because the beam size of our data ( $27''.6$ ) is smaller than that of their data ( $55''$ , which suffers more from the beam dilution effect because the angular size of the source is smaller than the beam size).

To estimate the column densities of other molecular species, we make two assumptions on their  $T_{\text{ex}}$ : (1) assuming that  $T_{\text{ex}}$  of other species are equal to  $T_{\text{ex}}(\text{CO})$ , and (2) fixing  $T_{\text{ex}} = 5 \text{ K}$  (van der Tak et al. 2007) throughout the target region for other species because they trace denser gas compared with CO (Shirley 2015). We do not estimate the column density of  $\text{H}_2\text{CO}$  because of the low signal-to-noise ratio of its transition. The abundance ratio maps of  $N(\text{HCO}^+)/N(\text{CO})$ ,  $N(\text{HCN})/N(\text{CO})$ ,  $N(\text{C}_2\text{H})/N(\text{CO})$ , and  $N(o\text{-}c\text{-C}_3\text{H}_2)/N(\text{CO})$  based on the two assumptions are separately shown in Figure 5. Here we cannot obtain the abundances of  $\text{HCO}^+$ ,  $\text{HCN}$ ,  $\text{C}_2\text{H}$  and  $o\text{-}c\text{-C}_3\text{H}_2$  because the abundance of CO is not necessarily  $\sim 10^{-4}$  at such low column densities (e.g., Burgh et al. 2007).

As can be seen in Figure 5, the difference between the abundance ratios estimated for the two assumed cases of  $T_{\text{ex}}$  is within a factor of 2 for  $\text{HCO}^+$ ,  $\text{HCN}$  and  $\text{C}_2\text{H}$ , and a factor of 3 for  $o\text{-}c\text{-C}_3\text{H}_2$ . The obtained ranges of the abundance ratios, including the values obtained with the two assumptions, are  $1.0$ – $4.0 \times 10^{-4}$ ,  $1.8$ – $5.3 \times 10^{-4}$ ,  $1.6$ – $5.0 \times 10^{-3}$ , and  $1.2$ – $7.9 \times 10^{-4}$  for  $N(\text{HCO}^+)/N(\text{CO})$ ,  $N(\text{HCN})/N(\text{CO})$ ,  $N(\text{C}_2\text{H})/N(\text{CO})$ , and  $N(o\text{-}c\text{-C}_3\text{H}_2)/N(\text{CO})$ , respectively. The abundance ratios are all highest toward the eastern edge of the molecular clump and decrease toward the west, which is roughly consistent with the direction of the SNR blast wave.

<sup>5</sup> <https://splatalogue.online/>

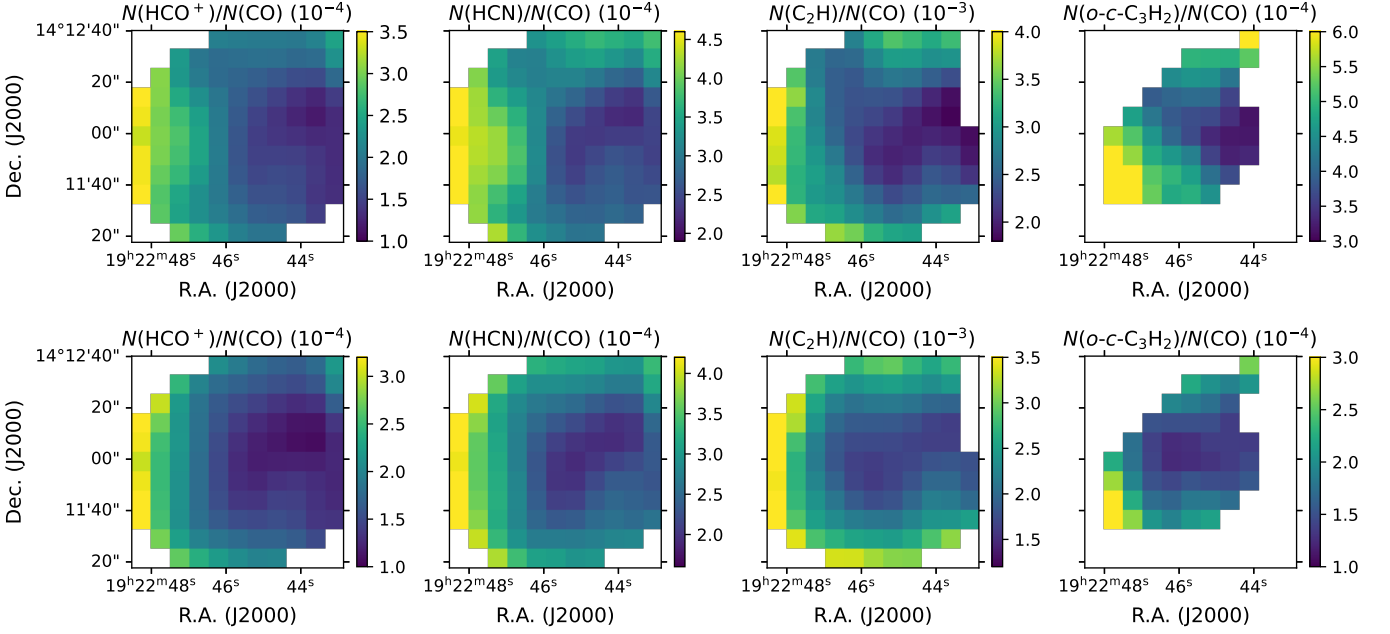


**Fig. 5.** Maps of abundance ratios  $N(\text{HCO}^+)/N(\text{CO})$ ,  $N(\text{HCN})/N(\text{CO})$ ,  $N(\text{C}_2\text{H})/N(\text{CO})$ , and  $N(o\text{-}c\text{-C}_3\text{H}_2)/N(\text{CO})$  (from left to right) based on the assumptions  $T_{\text{ex}} = T_{\text{ex}}(\text{CO})$  (upper row) and  $T_{\text{ex}} = 5 \text{ K}$  (lower row).

We also estimate an upper limit of the  $N(\text{C}^0)/N(\text{CO})$  considering that no broadened [C I] emission (See Section 2.2) is detected. The upper limit of  $N(\text{C}^0)$  can be estimated with (Izumi et al. 2021):

$$N(\text{C}^0) = 4.67 \times 10^{16} \times \frac{1 + 3 \exp(-23.6/T_{\text{ex}}) + 5 \exp(-62.5/T_{\text{ex}})}{1 - \exp(-23.6/T_{\text{ex}})} \int \tau_{[\text{C I}]} dv \quad (3)$$

where the optical depth of the [C I] line is:

$$\tau_{[\text{C I}]} = -\ln \left[ 1 - \frac{T_{\text{mb}}}{J_{\nu}(T_{\text{ex}}) - J_{\nu}(T_{\text{bg}})} \right]. \quad (4)$$

We assume that the non-detected [C I] line profile follows a Gaussian with a full width at half maximum (FWHM)  $15 \text{ km s}^{-1}$ . We smooth the original data to a beam of  $27''.6$  (see Section 2.2) and a velocity channel width of  $3 \text{ km s}^{-1}$ . The  $3\sigma$  upper limit of the  $T_{\text{mb}}$  is  $0.5 \text{ K}$ . We vary the  $T_{\text{ex}}$  from  $12 \text{ K}$  to  $22 \text{ K}$  to find the maximum upper limit of  $N(\text{C}^0)$ . Finally, we find an upper limit for  $N(\text{C}^0)/N(\text{CO})$  is  $\leq 2$ .

#### 4.2. Constraint on the gas density

Although we cannot conduct non-LTE analysis to fit the physical parameters of the molecular clump, we can still constrain its gas density. The peak integrated intensity of the  $\text{HCO}^+ J = 1-0$  line is  $\approx 12 \text{ K km s}^{-1}$  (which is inferred by combining Figure 3 (e) and (f)), and the peak  $N(\text{HCO}^+)$  in the LTE analysis is  $\sim 2 \times 10^{13} \text{ cm}^{-2}$  (which is inferred by combining Figure 4 and 5). We note that although the LTE analysis is indeed not precise, we consider  $N(\text{HCO}^+)$  for two cases of  $T_{\text{ex}}$  of  $5 \text{ K}$  and  $\sim 20 \text{ K}$  as the lower and upper ends of the  $T_{\text{ex}}$  range separately. Therefore, the estimated peak can be regarded as a strict upper limit of the real  $N(\text{HCO}^+)$ . To constrain the gas density, we run a set of physical parameters with the non-LTE radiative transfer code, RADEX

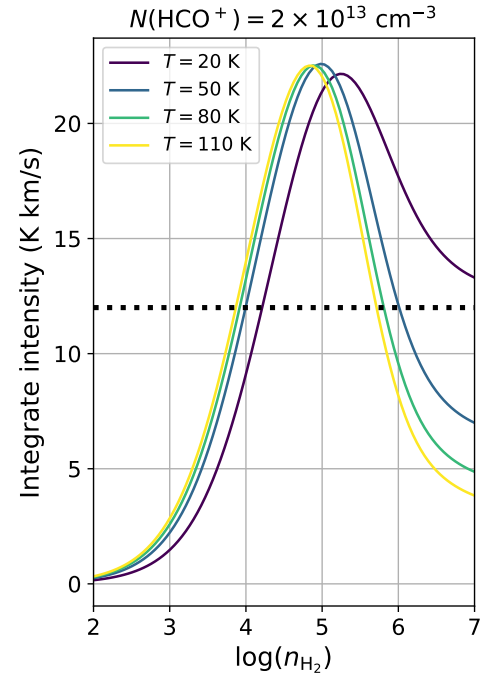


**Fig. 6.** The predicted integrated intensity of  $\text{HCO}^+ J = 1-0$  line as a function of  $n_{\text{H}_2}$ . The lines with different colors show the models with different gas temperatures. The dotted black line in the right panel shows an integrated intensity of  $12 \text{ K km s}^{-1}$ .

(van der Tak et al. 2007), varying the gas density  $n_{\text{H}_2}$  and gas temperature  $T$  with fixed  $N(\text{HCO}^+) = 2 \times 10^{13} \text{ cm}^{-2}$  and an FWHM of  $15 \text{ km s}^{-1}$ . Similar method has been used by Shirley (2015) to estimate the “effective excitation density” of dense gas tracers. We plot the predicted relation between integrated intensity and the gas density at given values of  $T$  in Figure 6. We find that the gas density should be at least  $\sim 10^4 \text{ cm}^{-3}$  to reproduce the observed peak intensity of the  $\text{HCO}^+ J = 1-0$  line. Although



higher gas temperature also enhance the integrated intensity at  $n_{\text{H}_2} \lesssim 10^5 \text{ cm}^{-3}$ , this effect is not significant at  $T \gtrsim 50 \text{ K}$ .

#### 4.3. Unusual $N(\text{C}_2\text{H})/N(\text{CO})$ and $N(o\text{-}c\text{-C}_3\text{H}_2)/N(\text{CO})$ abundance ratios

We recall that the estimated abundance ratio is of order  $\sim 10^{-3}$  for  $N(\text{C}_2\text{H})/N(\text{CO})$  and  $\sim 10^{-4}$  for  $N(o\text{-}c\text{-C}_3\text{H}_2)/N(\text{CO})$ . In dense quiescent MCs, these ratios are typically  $\sim 10^{-4}$ – $10^{-5}$  and  $\sim 10^{-5}$ – $10^{-6}$ , respectively (e.g., Agúndez & Wakelam 2013; Kim et al. 2020). Therefore, the obtained  $N(\text{C}_2\text{H})/N(\text{CO})$  and  $N(o\text{-}c\text{-C}_3\text{H}_2)/N(\text{CO})$  ratios are higher than the typical values in dense MCs by 1–2 orders of magnitude.

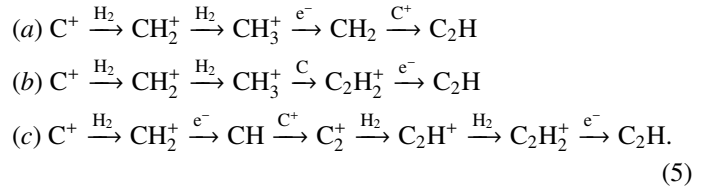
Broadened emission line induced by SNR-MC interaction of  $\text{C}_2\text{H}$  has only been found in SNRs IC443 (van Dishoeck et al. 1993), W28 (Mazumdar et al. 2022) and 3C391 (Tu et al. 2024b), while broadened  $c\text{-C}_3\text{H}_2$  line has only been found in SNR 3C391 (Tu et al. 2024b). The  $N(\text{C}_2\text{H})/N(\text{CO})$  toward IC443 clump G, which is one of the prototypical molecular clumps interacting with SNRs, is  $\sim 10^{-4}$  (van Dishoeck et al. 1993), similar to the value in typical quiescent MCs. In other environments of interstellar shocks,  $\text{C}_2\text{H}$  and  $c\text{-C}_3\text{H}_2$  are also seldom discussed. For example, these two species are regarded as tracers of ambient gas (e.g., Shimajiri et al. 2015) or cavity walls exposed to UV radiation (e.g., Tychoniec et al. 2021) in protostellar outflows. In molecular cloud core L1521, which is a source of shocked carbon chain chemistry with enhanced abundance of some carbon chain species, the abundance ratio  $N(c\text{-C}_3\text{H}_2)/N(\text{CO})$  is  $\sim 10^{-5}$  (Sato et al. 1994; Liu et al. 2021). We note that the ortho-to-para ratio of  $c\text{-C}_3\text{H}_2$  is 3 in thermal equilibrium and is often observed to be within the range of 1–3 (Park et al. 2006). Therefore, the column density of  $o\text{-}c\text{-C}_3\text{H}_2$  should be similar to that of  $c\text{-C}_3\text{H}_2$ , and the observed  $N(c\text{-C}_3\text{H}_2)/N(\text{CO})$  value toward L1251 is lower than the value we obtained in W51C by an order of magnitude.

Enhanced  $N(\text{C}_2\text{H})/N(\text{CO})$  ratio similar to our case was found in the circumnuclear disk of Seyfert galaxy NGC 1068 (Viti et al. 2014; Nakajima et al. 2023), but it was proposed to be the results of a complex interaction with shock and UV or X-ray radiation (García-Burillo et al. 2017).

Our observed abundance ratios are roughly consistent with the values in diffuse or translucent molecular gas: Liszt & Lucas (1998) for CO, Lucas & Liszt (1996) for  $\text{HCO}^+$ , Liszt & Lucas (2001) for HCN, and Lucas & Liszt (2000) for  $\text{C}_2\text{H}$  and  $c\text{-C}_3\text{H}_2$ . See also Table 3 of Liszt et al. (2006) for a compilation. We also refer to Kim et al. (2023) for a later observation of all the species except CO. However, the gas density of the target clump ( $\gtrsim 10^4 \text{ cm}^{-3}$ ) is higher than the typical values of diffuse and translucent clouds (Snow & McCall 2006). Therefore, the dominating physical and chemical processes are expected to be different.

Carbon chain species, including  $\text{C}_2\text{H}$  and  $c\text{-C}_3\text{H}_2$ , are regarded as “early-type species” (Sakai & Yamamoto 2013; Taniguchi et al. 2024). The formation of carbon chain species rely strongly on  $\text{C}^+$  and  $\text{C}^0$  in the gas phase (see Figure 1 of Sakai & Yamamoto (2013) and Figure 1 of Taniguchi et al. (2024)), which are transformed to CO as the cloud evolves from diffuse gas to molecular cloud core. For instance, the formation routes

of  $\text{C}_2\text{H}$  include but are not limited to (Taniguchi et al. 2024):



Therefore, carbon chains are formed efficiently at the earliest phase of MC formation and are depleted or destructed in evolved MCs, which has been verified by many chemical simulations (e.g., Suzuki et al. 1992; Taniguchi et al. 2019). Since the target clump is molecular gas re-formed behind a dissociative J-shock, it is supposed to be at the earliest phase of MC evolution with abundant  $\text{C}^+$  and  $\text{C}^0$  in the gas phase. Therefore, enhanced abundances of carbon chain species, and in turn their abundance ratios to CO, are possible. Simulation of Neufeld & Dalgarno (1989) also predict a plateau of  $\text{C}_2\text{H}$  abundance  $X(\text{C}_2\text{H})$  soon after the J-shock. However, this simulation only considered fast J-shock in dense preshock gas  $> 10^4 \text{ cm}^{-3}$  which is higher than the preshock density in our case, and did not either predict significantly enhanced  $N(\text{C}_2\text{H})/N(\text{CO})$  abundance ratio.

#### 4.4. Chemical simulation of molecular re-formation behind J-shock

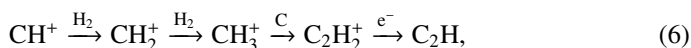
To further investigate whether the enhanced  $N(\text{C}_2\text{H})/N(\text{CO})$  and  $N(o\text{-}c\text{-C}_3\text{H}_2)/N(\text{CO})$  abundance ratios are due to the chemistry induced by J-shock, we use the Paris-Durham shock code (Flower et al. 1985; Flower & Pineau des Forêts 2003, 2015; Godard et al. 2019) to simulate the molecular re-formation behind J-shock. The code is a public numerical tool to compute the coupled dynamical, thermal, and chemical evolution of interstellar medium subject to plane parallel shock wave. The computation consists of two steps. In step 1, the code simulates the evolution of a quiescent cloud and evolve into a steady state. In step 2, the code uses the outputs of step 1 as the preshock conditions (including both physical and chemical parameters) and allows a shock wave to propagate into the preshock cloud.

We simulate both irradiated and non-irradiated shocks. In the irradiated case, we assume that a cloud with a visual extinction of  $A_V = 2$  (at the interface between translucent and dense MC (Snow & McCall 2006)) is irradiated by the interstellar radiation field with  $G_0 = 1.6$  in the Habing unit<sup>6</sup> (Parravano et al. 2003; Wolfire et al. 2022). The magnetic field in the simulation is controlled by a parameter  $\beta = B(\mu\text{G})/\sqrt{n_{\text{H}}(\text{cm}^{-3})}$ . We adopt  $\beta = 1$  which is close to the magnetic field in interstellar clouds (Crutcher et al. 2010). The cosmic-ray ionization rate per  $\text{H}_2$  is fixed to be  $1.3 \times 10^{-17} \text{ s}^{-1}$  in step 1, which is the typical value in MCs (Caselli et al. 1998), and is enhanced to  $5 \times 10^{-16} \text{ s}^{-1}$  in step 2, roughly consistent with previous observations and simulations (Ceccarelli et al. 2011; Shingledecker et al. 2016; Yamagishi et al. 2023). The propagation time of the shock is limited to  $t < 3 \times 10^4 \text{ yr}$ , which is consistent with previous constraint on the age of W51C (Koo et al. 1995; Park et al. 2013). We vary the preshock H nucleus density  $n_{\text{H}}$  to be  $2 \times 10^2$ ,  $2 \times 10^3$  and  $2 \times 10^4 \text{ cm}^{-3}$ , and shock velocity  $V_s$  to be 25, 30, 40, 50 and 60  $\text{km s}^{-1}$ . At lower  $V_s$ , the shock becomes C-shock. We find that the preshock density  $n_{\text{H}} = 2 \times 10^3 \text{ cm}^{-3}$  can better reproduce the observed abundance ratio and the results that the target clump

<sup>6</sup>  $G_0 = 1$  indicates an integrated flux of  $1.6 \times 10^{-3} \text{ erg cm}^{-2} \text{ s}^{-1}$  in 6–13.6 eV.

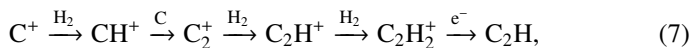
has a density  $n_{\text{H}_2} \gtrsim 10^4 \text{ cm}^{-3}$ . Therefore we limit our discussion with  $n_{\text{H}} = 2 \times 10^3 \text{ cm}^{-3}$ .

Figure 7 shows the abundance ratios predicted by the non-irradiated (upper row) and irradiated (lower row) shock models. For the non-irradiated shock model, all of the four abundance ratios except  $N(\text{C}_2\text{H})/N(\text{CO})$  can be well reproduced, while the difference between the peak values of the modeled  $N(\text{C}_2\text{H})/N(\text{CO})$  and observed range is within an order of magnitude. Therefore, we conclude that the observed abundance ratio can essentially be reproduced by the J-shock chemistry. We note that the  $N(\text{C}_2\text{H})/N(\text{CO})$  and  $N(c\text{-C}_3\text{H}_2)/N(\text{CO})$  reach the peak values at  $\sim 3 \times 10^3 \text{ yr}$ , and then quickly decrease. This is consistent with the scenario that the carbon chain species are “early-type species” and are destructed along with the evolution of the MC (Sakai & Yamamoto 2013; Taniguchi et al. 2024). Specifically,  $\text{C}_2\text{H}$  is mainly formed via:



at  $t \lesssim 3 \text{ kyr}$ , where the  $\text{CH}^+$  can be formed through either  $\text{C}^+ + \text{H}_2$  or  $\text{C} + \text{H}_3^+$ . This pathway is similar to route (b) mentioned in reactions 5. Atomic C, which is key to the formation of  $\text{C}_2\text{H}_2^+$ , is formed in the J-shock through the dissociation of CO and CH. At  $t \gtrsim 3 \text{ kyr}$ ,  $\text{C}_2\text{H}$  is mainly destructed by atomic O to form CO. The formation of  $c\text{-C}_3\text{H}_2$  is much more complicated, ended with  $c\text{-C}_3\text{H}_3^+ + e^- \rightarrow c\text{-C}_3\text{H}_2 + \text{H}$ , where the  $c\text{-C}_3\text{H}_3^+$  molecule can be formed via  $c\text{-C}_3\text{H}^+ / c\text{-C}_3\text{H}_2^+ + \text{H}_2$ .

For the irradiated shock model, the  $N(\text{HCO}^+)/N(\text{CO})$  and  $N(\text{C}_2\text{H})/N(\text{CO})$  can be well reproduced, while the  $N(c\text{-C}_3\text{H}_2)/N(\text{CO})$  is within an order of magnitude away from the observed range. However, the  $N(\text{HCN})/N(\text{CO})$  is strongly overestimated by the irradiated model. Therefore, although this model can roughly reproduce the observed abundance ratios, its performance is worse than the non-irradiated shock model. The formation pathway of  $\text{C}_2\text{H}$  in the irradiated shock model is slightly different from that in the non-irradiated shock model:



because of the higher abundance of C and  $\text{C}^+$  due to the external UV field.

We note that although both models can reproduce the observed abundance ratios to some extent, the simulation is not exempt from problems. We recall that there are some other constraints on the physical properties of the target molecular clump. Koo & Moon (1997b) found that the abundance ratio  $N(\text{CO})/N(\text{HI})$  is  $< 4 \times 10^{-5}$ , which is the expected value if CO has totally been re-formed while HI has yet to form  $\text{H}_2$ . To explain this effect, they proposed that the hydrogen nuclei are mainly in the atomic form instead of molecular form according to the  $N(\text{HI})$  vs.  $N(\text{CO})$  scatter plot (see their Figure 5). However, as plotted in the left panel of Figure 8, a significant fraction of H has recombined to  $\text{H}_2$  even before  $2 \times 10^3 \text{ yr}$  regardless of shock velocity in the non-irradiated shock models. Therefore, the non-irradiated shock models can hardly reproduce the trends proposed by Koo & Moon (1997b). On the other hand, for the irradiated models, the  $N(\text{CO})/N(\text{HI}) < 4 \times 10^{-5}$  can be naturally explained by the fact that neither CO nor  $\text{H}_2$  has been remarkably re-formed (see the middle panel of Figure 8). But in Section 4.1 we obtain an upper limit for the  $N(\text{C}^0)/N(\text{CO})$  abundance ratio  $\lesssim 2$ . However, the irradiated shock models may have significantly overestimated the  $N(\text{C}^0)/N(\text{CO})$  abundance ratio because of the photodissociation of incident UV radiation. This could be because the target clump suffers from a less intense UV field

compared with our assumption. An alternative explanation is the uncertainty in the treatment of UV radiative transfer in the shock model as shown in Godard et al. (2019).

In summary, our illustrative simulation can essentially reproduce, despite some defects, the observed abundance ratios, especially the enhanced  $N(\text{C}_2\text{H})/N(\text{CO})$  and  $N(c\text{-C}_3\text{H}_2)/N(\text{CO})$ . This suggests that these abundance ratios can be explained by the chemistry induced by the J-shock. However, we also note that the chemical simulation is not exempt from problems such as the lack of consideration of three-dimensional structure of the MC and incomplete chemical network. In addition, we only investigate some specific cases with simple assumptions on the properties such as UV field, magnetic field, and CR ionization rate, instead of exploring the full parameter space. Further improvement on the chemical network, especially the grain-surface chemistry that strongly affects the initial condition of the shock and plays an important role in carbon-chain chemistry (Sakai & Yamamoto 2013), and the treatment of UV radiative transfer may be helpful for the shock model to better reproduce the observation, but this is beyond the scope of this paper.

## 5. Conclusions

We present new observation toward W51C clump 2 in 71.4–89.7 GHz with the Yebes 40 m radio telescope to study the molecular chemistry induced by J-shock. Five molecular species ( $\text{HCO}^+$ , HCN,  $\text{C}_2\text{H}$ ,  $o\text{-}c\text{-C}_3\text{H}_2$ , and  $\text{H}_2\text{CO}$ ) exhibit broadened emission line profiles in  $+80\text{--}+110 \text{ km s}^{-1}$  which is the velocity range of the re-formed molecular gas behind J-shock. We find that the spectrum of  $\text{HCO}^+ J = 1\text{--}0$  can be divided into six velocity components, in which the re-formed gas can be divided into two components with different spatial distribution. To facilitate the analysis, we regard the two re-formed gas components as one.

With the CO  $J = 1\text{--}0$  and  $3\text{--}2$  data, we estimate the excitation temperature and column density of CO based on the LTE assumption, and obtain the abundance ratios of  $\text{HCO}^+$ , HCN,  $\text{C}_2\text{H}$ ,  $o\text{-}c\text{-C}_3\text{H}_2$  to CO, which are  $N(\text{HCO}^+)/N(\text{CO}) \sim (1.0\text{--}4.0) \times 10^{-4}$ ,  $N(\text{HCN})/N(\text{CO}) \sim (1.8\text{--}5.3) \times 10^{-4}$ ,  $N(\text{C}_2\text{H})/N(\text{CO}) \sim (1.6\text{--}5.0) \times 10^{-3}$ , and  $N(o\text{-}c\text{-C}_3\text{H}_2)/N(\text{CO}) \sim (1.2\text{--}7.9) \times 10^{-4}$ . We also obtain an upper limit for the  $N(\text{C}^0)/N(\text{CO})$  abundance ratio  $\lesssim 2$ . We find that the  $N(\text{C}_2\text{H})/N(\text{CO})$  and  $o\text{-}c\text{-C}_3\text{H}_2$  ratios are higher than the typical values in dense MCs and the value in SNR IC443 clump G. This enhancement can be qualitatively attributed to the chemistry at the earliest phase of MC formation when abundant  $\text{C}^+$  and C in the gas phase boost the formation of carbon chain species.

To further investigate whether the enhanced  $N(\text{C}_2\text{H})/N(\text{CO})$  and  $N(c\text{-C}_3\text{H}_2)/N(\text{CO})$  are due to J-shock chemistry, we conduct a chemical simulation with the Paris-Durham shock code. We find that both the non-irradiated and the irradiated shock models with a preshock density of  $n_{\text{H}} = 2 \times 10^3 \text{ cm}^{-3}$  can basically reproduce the observed abundance ratios despite some defects, which suggests that the abundance ratios can indeed be attributed to the chemistry induced by J-shock. However, the non-irradiated models overestimate the re-formation of  $\text{H}_2$ , while the irradiated models overestimate the  $N(\text{C}^0)/N(\text{CO})$  abundance ratio. Improvements on the shock code may be helpful for reproducing the observation.

*Acknowledgements.* The authors thank Alba Vidal García who carried out the observations and the first inspection of the data quality, other staff of the Yebes observatory who supported the observation and data transmission, Mitsuyoshi Yamagishi who provided the data cubes of  $^{12}\text{CO}$  and [C I], and Benjamin Godard who offered helps on the use of the Paris-Durham shock code. V.W. acknowledges the CNRS program “Physique et Chimie du Milieu Interstellaire” (PCMI)

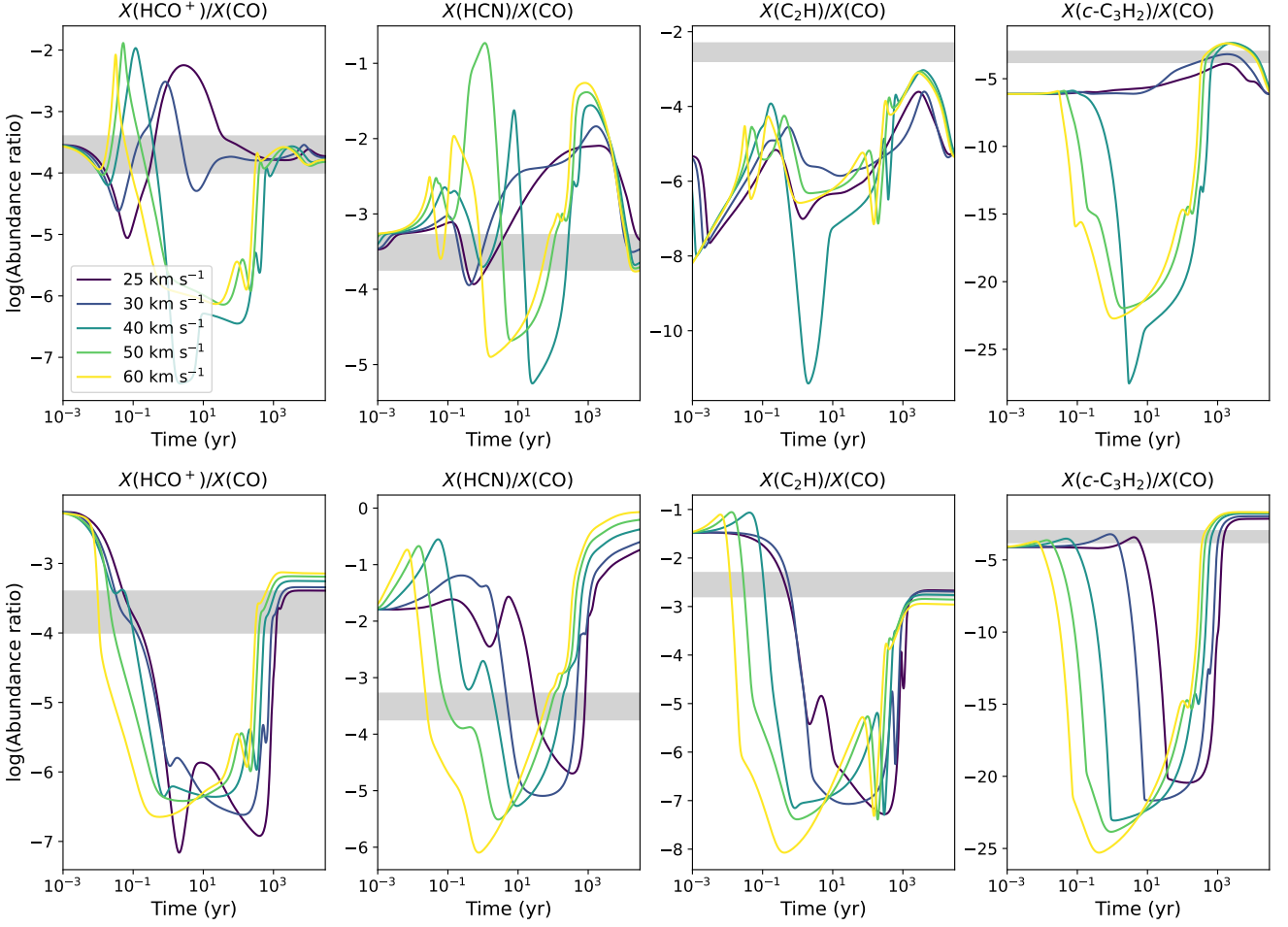


**Fig. 7.** Abundance ratios  $N(\text{HCO}^+)/N(\text{CO})$ ,  $N(\text{HCN})/N(\text{CO})$ ,  $N(\text{C}_2\text{H})/N(\text{CO})$  and  $N(c\text{-C}_3\text{H}_2)/N(\text{CO})$  (from left to right) predicted by the Paris-Durham shock code as a function of time with a preshock density of  $n_{\text{H}} = 2 \times 10^3 \text{ cm}^{-3}$ . The upper row shows the results of non-irradiated shock, while the lower row shows the results of shock irradiated by an interstellar radiation field ( $G_0 = 1.6$ ) with a visual extinction of  $A_V = 2$ . Lines with different colors shows the results of different shock velocities as shown in the labels of the upper right panel. The gray shaded regions delineate the range obtained from our observation.

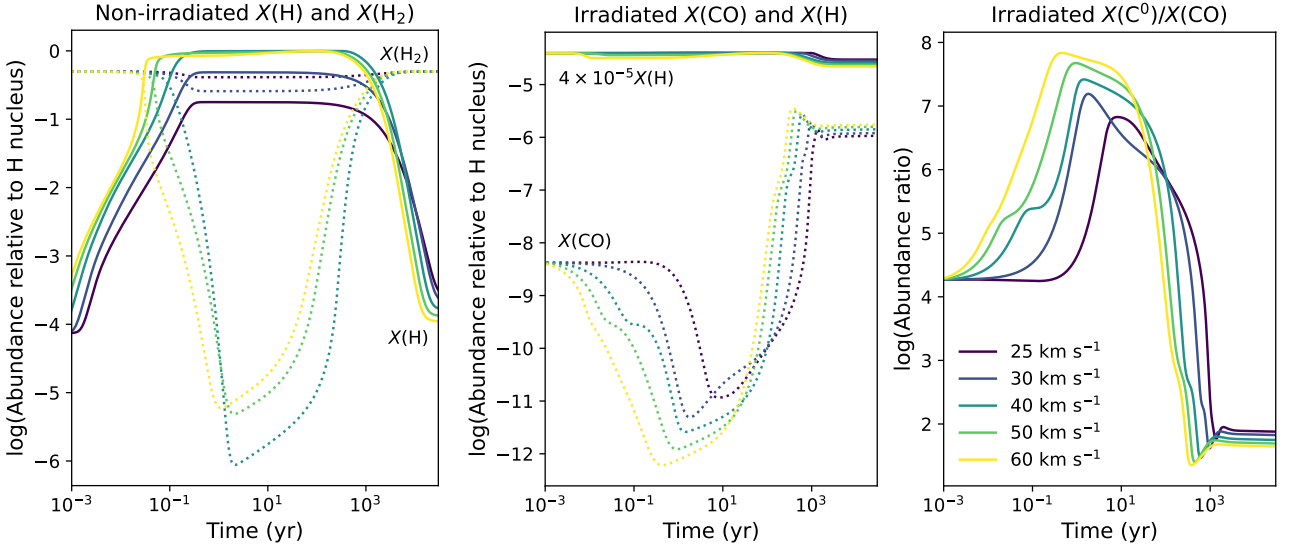


**Fig. 8.** Auxiliary results of the non-irradiated (left panel) and irradiated (middle and right panel) shock models with a preshock density of  $n_{\text{H}} = 2 \times 10^3 \text{ cm}^{-3}$ . Lines with different colors shows the results of different shock velocity as shown in the labels of the right panel. *left panel:* Evolution of the abundances (denoted by  $X$ ) of H (solid lines) and  $\text{H}_2$  (dotted lines) relative to the total H nucleus in the non-irradiated models. *middle panel:* Evolution of the abundances of H (solid lines, multiplied by a factor of  $4 \times 10^{-5}$ ) and CO (dotted lines) relative to the total H nucleus in the irradiated models. *right panel:* Evolution of the abundance ratio  $N(\text{C}^0)/N(\text{CO})$  in the irradiated models.



co-funded by the Centre National d'Etudes Spatiales (CNES). Y.C. acknowledges the support from NSFC grants Nos. 12173018 and 12121003. P.Z. acknowledges the support from NSFC grant No. 12273010. This article is based on observations carried out with the Yebes 40 m telescope (project code: 24A003). The 40 m radio telescope at Yebes Observatory is operated by the Spanish Geographic Institute (IGN; Ministerio de Transportes y Movilidad Sostenible). This work has made use of the Paris-Durham public shock code V1.1, distributed by the CNRS-INSU National Service "ISM Platform" at the Paris Observatory Data Center (<http://ism.obspm.fr>).

## References

- Agúndez, M. & Wakelam, V. 2013, *ChRv*, 113, 8710
- Astropy Collaboration, Price-Whelan, A. M., Lim, P. L., et al. 2022, *ApJ*, 935, 167
- Astropy Collaboration, Price-Whelan, A. M., Sipőcz, B. M., et al. 2018, *ApJ*, 156, 123
- Bachiller, R., Pérez Gutiérrez, M., Kumar, M. S. N., & Tafalla, M. 2001, *A&A*, 372, 899
- Benedettini, M., Busquet, G., Lefloch, B., et al. 2012, *A&A*, 539, L3
- Brogan, C. L., Goss, W. M., Hunter, T. R., et al. 2013, *ApJ*, 771, 91
- Burgh, E. B., France, K., & McCandliss, S. R. 2007, *ApJ*, 658, 446
- Burkhardt, A. M., Shingledecker, C. N., Le Gal, R., et al. 2019, *ApJ*, 881, 32
- Caselli, P., Walmsley, C. M., Terzieva, R., & Herbst, E. 1998, *ApJ*, 499, 234
- Ceccarelli, C., Hily-Blant, P., Montmerle, T., et al. 2011, *ApJ*, 740, L4
- Codella, C., Ceccarelli, C., Bianchi, E., et al. 2020, *A&A*, 635, A17
- Crutcher, R. M., Wandelt, B., Heiles, C., Falgarone, E., & Troland, T. H. 2010, *ApJ*, 725, 466
- Cuppen, H. M., Kristensen, L. E., & Gavardi, E. 2010, *MNRAS*, 406, L11
- Draine, B. T. & McKee, C. F. 1993, *ARA&A*, 31, 373
- Dumas, G., Vaupré, S., Ceccarelli, C., et al. 2014, *ApJ*, 786, L24
- Flower, D. R. & Pineau des Forêts, G. 2003, *MNRAS*, 343, 390
- Flower, D. R. & Pineau des Forêts, G. 2015, *A&A*, 578, A63
- Flower, D. R., Pineau des Forêts, G., & Hartquist, T. W. 1985, *MNRAS*, 216, 775
- García-Burillo, S., Viti, S., Combes, F., et al. 2017, *A&A*, 608, A56
- Godard, B., Pineau des Forêts, G., Lesaffre, P., et al. 2019, *A&A*, 622, A100
- Goldsmith, P. F. & Langer, W. D. 1999, *ApJ*, 517, 209
- Gómez-Ruiz, A. I., Codella, C., Lefloch, B., et al. 2015, *MNRAS*, 446, 3346
- Green, A. J., Frail, D. A., Goss, W. M., & Otrupcek, R. 1997, *ApJ*, 114, 2058
- Green, D. A. 2019, *JApA*, 40, 36
- Gusdorf, A., Cabrit, S., Flower, D. R., & Pineau Des Forêts, G. 2008, *A&A*, 482, 809
- Hollenbach, D., Elitzur, M., & McKee, C. F. 2013, *ApJ*, 773, 70
- Hollenbach, D. & McKee, C. F. 1989, *ApJ*, 342, 306
- Izumi, N., Fukui, Y., Tachihara, K., et al. 2021, *PASJ*, 73, 174
- Kim, W. J., Schilke, P., Neufeld, D. A., et al. 2023, *A&A*, 670, A111
- Kim, W. J., Wyrowski, F., Urquhart, J. S., et al. 2020, *A&A*, 644, A160
- Koo, B.-C., Kim, K.-T., & Seward, F. D. 1995, *ApJ*, 447, 211
- Koo, B.-C. & Moon, D.-S. 1997a, *ApJ*, 475, 194
- Koo, B.-C. & Moon, D.-S. 1997b, *ApJ*, 485, 263
- Kristensen, L. E., Godard, B., Guillard, P., Gusdorf, A., & Pineau des Forêts, G. 2023, *A&A*, 675, A86
- Lazendic, J. S., Wardle, M., Whiteoak, J. B., Burton, M. G., & Green, A. J. 2010, *MNRAS*, 409, 371
- Lee, Y.-H., Koo, B.-C., Lee, J.-J., Burton, M. G., & Ryder, S. 2019, *ApJ*, 157, 123
- Lefloch, B., Cabrit, S., Busquet, G., et al. 2012, *ApJ*, 757, L25
- Liszt, H. & Lucas, R. 2001, *A&A*, 370, 576
- Liszt, H. S. & Lucas, R. 1998, *A&A*, 339, 561
- Liszt, H. S., Lucas, R., & Pety, J. 2006, *A&A*, 448, 253
- Liu, X. C., Wu, Y., Zhang, C., et al. 2021, *ApJ*, 912, 148
- Lucas, R. & Liszt, H. 1996, *A&A*, 307, 237
- Lucas, R. & Liszt, H. S. 2000, *A&A*, 358, 1069
- Mangum, J. G. & Shirley, Y. L. 2015, *PASA*, 127, 266
- Mazumdar, P., Tram, L. N., Wyrowski, F., Menten, K. M., & Tang, X. 2022, *A&A*, 668, A180
- Mendoza, E., Lefloch, B., Ceccarelli, C., et al. 2018, *MNRAS*, 475, 5501
- Nakajima, T., Takano, S., Tosaki, T., et al. 2023, *ApJ*, 955, 27
- Neufeld, D. A. & Dalgarno, A. 1989, *ApJ*, 340, 869
- Park, G., Currie, M. J., Thomas, H. S., et al. 2023, *ApJS*, 264, 16
- Park, G., Koo, B. C., Gibson, S. J., et al. 2013, *ApJ*, 777, 14
- Park, I. H., Wakelam, V., & Herbst, E. 2006, *A&A*, 449, 631
- Parravano, A., Hollenbach, D. J., & McKee, C. F. 2003, *ApJ*, 584, 797
- Rho, J., Hewitt, J. W., Boogert, A., Kaufman, M., & Gusdorf, A. 2015, *ApJ*, 812, 44
- Rho, J., Jarrett, T. H., Cutri, R. M., & Reach, W. T. 2001, *ApJ*, 547, 885
- Sakai, N. & Yamamoto, S. 2013, *ChRv*, 113, 8981
- Sato, F., Mizuno, A., Nagahama, T., et al. 1994, *ApJ*, 435, 279
- Shimajiri, Y., Sakai, T., Kitamura, Y., et al. 2015, *ApJS*, 221, 31
- Shingledecker, C. N., Bergner, J. B., Le Gal, R., et al. 2016, *ApJ*, 830, 151
- Shinn, J.-H., Lee, H.-G., & Moon, D.-S. 2012, *ApJ*, 759, 34
- Shirley, Y. L. 2015, *PASP*, 127, 299
- Snow, T. P. & McCall, B. J. 2006, *ARA&A*, 44, 367
- Stil, J. M., Taylor, A. R., Dickey, J. M., et al. 2006, *AJ*, 132, 1158
- Suzuki, H., Yamamoto, S., Ohishi, M., et al. 1992, *ApJ*, 392, 551
- Taniguchi, K., Gorai, P., & Tan, J. C. 2024, *Ap&SS*, 369, 34
- Taniguchi, K., Herbst, E., Ozeki, H., & Saito, M. 2019, *ApJ*, 884, 167
- Tu, T.-y., Chen, Y., Zhou, P., Safi-Harb, S., & Liu, Q.-C. 2024a, *ApJ*, 966, 178
- Tu, T.-Y., Rayalacheruvu, P., Majumdar, L., et al. 2024b, *ApJ*, 974, 262
- Tychoniec, L., van Dishoeck, E. F., van't Hoff, M. L. R., et al. 2021, *A&A*, 655, A65
- Urquhart, J. S., König, C., Giannetti, A., et al. 2018, *MNRAS*, 473, 1059
- van der Tak, F. F. S., Black, J. H., Schöier, F. L., Jansen, D. J., & van Dishoeck, E. F. 2007, *A&A*, 468, 627
- van Dishoeck, E. F., Jansen, D. J., & Phillips, T. G. 1993, *A&A*, 279, 541
- Viti, S., García-Burillo, S., Fuente, A., et al. 2014, *A&A*, 570, A28
- Wang, Z. & Scoville, N. Z. 1992, *ApJ*, 386, 158
- Wolfire, M. G., Vallini, L., & Chevance, M. 2022, *ARA&A*, 60, 247
- Yamagishi, M., Furuya, K., Sano, H., et al. 2023, *PASJ*, 75, 883
- Zhou, P., Zhang, G.-Y., Zhou, X., et al. 2022, *ApJ*, 931, 144

Appendix A: Spectra of all other detected transitions

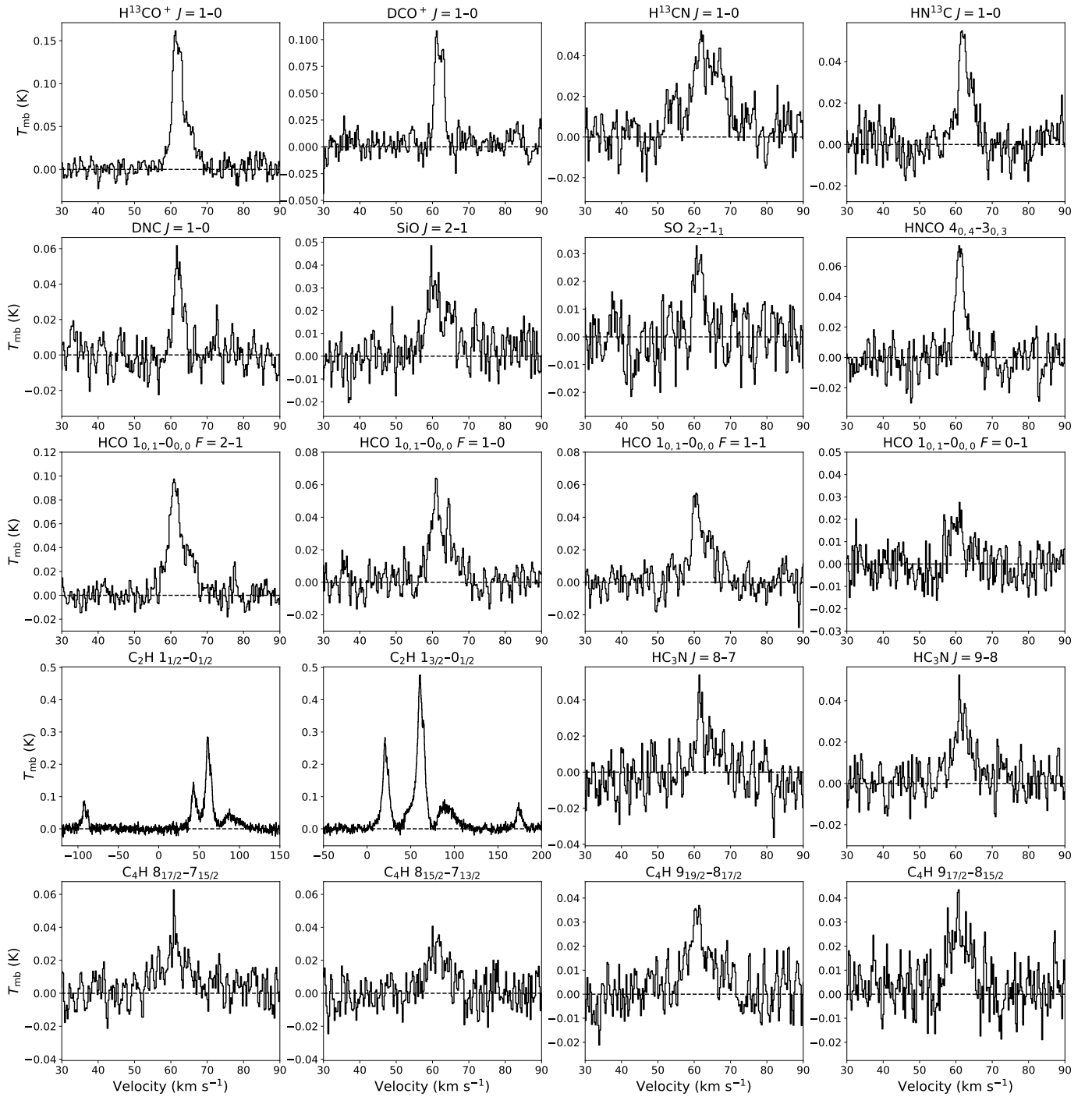
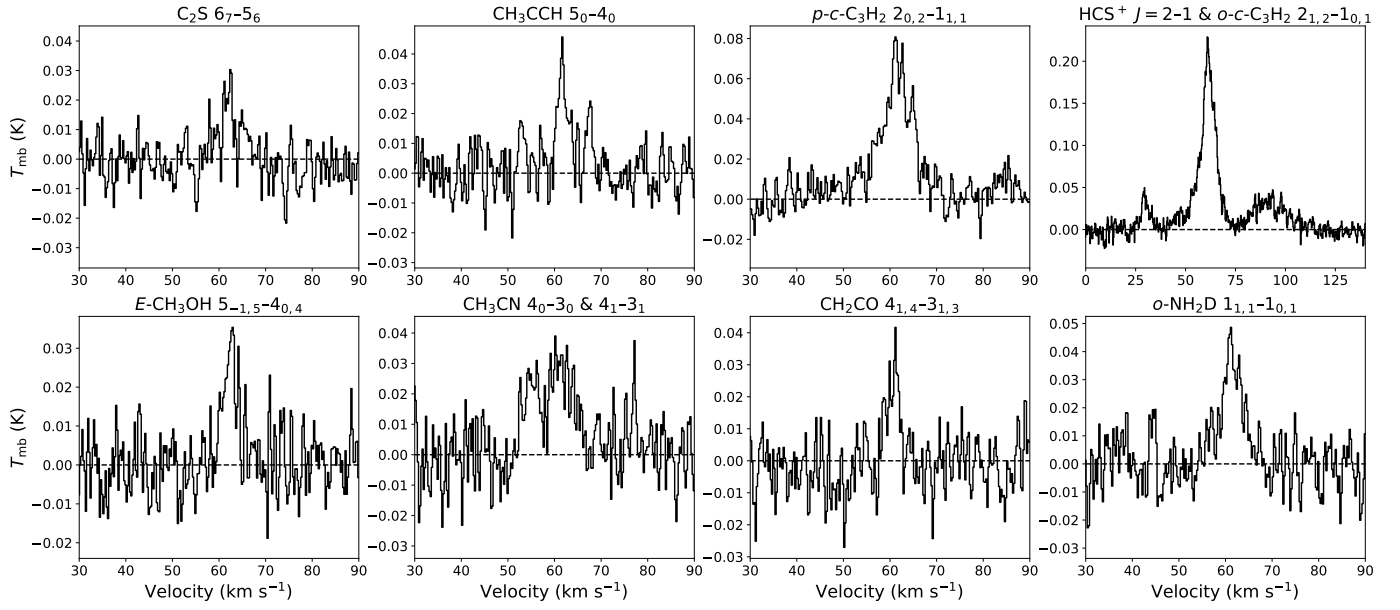


Fig. A.1. Spectra of all detected molecular transitions averaged in the entire field of view except those which have been shown in Figure 2.



**Fig. A.2.** *Continued.* The HCS<sup>+</sup>  $J = 2-1$  line is at  $\approx +29 \text{ km s}^{-1}$  in the upper right panel of which the rest frequency is set to be the frequency of the  $o-c\text{-C}_3\text{H}_2$  line.